Mon. Not. R. Astron. Soc. **000**, 1–10 (2015) Printed 18 June 2015 (MN LATEX style file v2.2)

Pulsar Lensing Geometry

Siqi Liu[1,3]⋆, Ue-Li Pen[1,2]†, J-P Macquart[4]‡, Walter Brisken[5]§, Adam Deller[6]¶
[1] *Canadian Institute for Theoretical Astrophysics, University of Toronto, M5S 3H8 Ontario, Canada*
[2] *Canadian Institute for Advanced Research, Program in Cosmology and Gravitation*
[3] *Department of Astronomy and Astrophysics, University of Toronto, M5S 3H4, Ontario, Canada*
[4] *ICRAR-Curtin University of Technology, Department of Imaging and Applied Physics, GPO Box U1978, Perth, Western Australia 6102, USA*
[5] *National Radio Astronomy Observatory, P.O. Box O, Socorro, NM 87801, USA*
[6] *ASTRON, the Netherlands Institute for Radio Astronomy, Postbus 2, 7990 AA, Dwingeloo, The Netherlands*

18 June 2015

ABSTRACT
By analysing archival VLBI data of PSR B0834+06, we conclude that for this example the plasma lenses can be precisely modelled using the inclined sheet model (Pen & Levin 2014), resulting in two distinct lens planes. This data strongly favours the grazing sheet model over turbulence as the primary source of pulsar scattering. 7 observed apex parameters fit the model to percent accuracy. Comparison with VLBI proper motion results in a direct measure of the ionized ISM screen. The results are consistent with motions expected in the local galaxy. The simple 1-D structure of the lenses opens up the possibility of using interstellar lenses as precision probes for pulsar lens mapping, precision transverse motions of the ISM, and new opportunities for removing scattering to improve pulsar timing. We describe the parameters and observables of this double screen system. While relative screen distances can in principle be accurately determined, a global conformal distance degeneracy exists which allows a rescaling of the absolute distance scale. This degeneracy is broken if the pulsar resides in a binary system, which is the case for most precision timing targets.

Key words: Pulsars: individual (B0834+06) – scattering – waves – magnetic: reconnection – techniques: interferometric – ISM: structure

1 INTRODUCTION

Pulsars have long provided a rich source of astrophysical information due to their compact emission and predictable timing. One of the weakest measurements for most pulsars is their direct geometric distance. For some pulsars, timing parallax or VLBI parallax has resulted in direct distance determination. For most pulsars, the distance is a major uncertainty for precision timing interpretations, including mass, moment of inertia (Kramer et al. 2006; Lorimer & Kramer 2012), and gravitational wave direction (Boyle & Pen 2012).

Direct VLBI observation of PSR B0834+06 shows multiple images lensed by the interstellar plasma. Combining the angular positions and scintillation delays, the authors published the derived effective distance (Brisken et al. 2010) (hereafter B10) of approximately 1168 ± 23 pc for apexes on the main scattering axis. This represents a precise measurement compared to all other attempts to derive distances to this pulsar. This effective distance is a combination of pulsar-screen and earth-screen distances, and does not allow a separate determination of the individual distances. A binary pulsar system would in principle allow a breaking of this degeneracy (Pen & Levin 2014). One potential limitation is the precision to which the lensing model can be understood.

In this paper, we examine the geometric nature of the lensing screens. In B10, VLBI astrometric mapping directly demonstrated the highly collinear nature of a single dominant lensing structure. First hints of single plane collinear dominated structure had been realized in Stinebring et al. (2001). While the nature of these structures are already mysterious, this puzzle is compounded by an offset group of lensed imaged called the 1 ms group. The mysterious nature of lensing questions any conclusions drawn from scintillometry as a quantitative tool (Pen et al. 2014).

Using archival data we demonstrate in this paper that the lensing screen consists of nearly parallel linear refractive structures, in two screens. The precise model confirms

⋆ E-mail: sqliu@cita.utoronto.ca
† E-mail: pen@cita.utoronto.ca
‡ E-mail:J.Macquart@curtin.edu.au
§ Email:wbrisken@aoc.nrao.edu
¶ E-mail:deller@astron.nl

the one dimensional nature, and thus the small number of parameters that quantify the lensing screen.

2 LENSING

In this section we map the data onto the grazing incidence sheet model. The folded sheet model is qualitatively analogous to the reflection of a light across a lake as seen from the opposite shore. In the absence of waves, exactly one image forms at the point where the angle of incidence is equal to the angle of reflection. In the presence of waves, one generically sees a line of images above and below the unperturbed image. The grazing angle geometry simplifies the lensing geometry, effectively reducing it from a two dimensional problem to one dimension. The statistics of such reflections is sometimes called glitter, and has many solvable properties (Longuet-Higgins 1960). This is illustrated in Fig. 1.

A similar effect occurs when the observer is below the surface. Two major distinctions arise: 1. the waves can deform the surface to create caustics in projection. Near caustics, Snell's law can lead to highly amplified refraction angles. 2. due to the odd image theorem, each caustic leads to two images. In practice, the surface could be caused be reconnection sheets (Braithwaite 2015), which have finite widths to regularize these singularities. Diffusive structures have Gaussian profiles, which was analysed in Pen & King (2012). The lensing details differ for convergent (underdense) vs divergent (over-dense) lenses, first considered by Clegg et al. (1998).

The generic interstellar electron density is insufficient to deflect radio waves by the observed $\sim$ mas bending angles. At grazing incidence, Snell's law results in an enhanced bending angle, which formally diverges. Magnetic discontinuities generically propagate as transverse surface waves, whose restoring force is the difference in Alfvén speed on the two sides of the discontinuity. This completes the analogy to waves on a lake: for sufficiently inclined sheets the waves will appear to fold back onto themselves in projection on the sky. At each fold caustic, Snell's law diverges, leading to enhanced refractive lensing. The divergence is cut off by a finite width of the sheet. The generic consequence is a series of collinear images. Each projected fold of the wave results in two density caustics. Each density caustic leads to two geometric lensing images, for a total of 4 images for each wave inflection. The two geometric image in each caustic are separated by the characteristic width of the sheet, if this is smaller than the Fresnel scale, the two images become effectively indistinguishable. The geometry of the inclined refractive lens is shown in Fig. 2.

A large number of sheets might intersect the line of sight to any pulsar. Only those sufficiently inclined would lead to caustic formation. Empirically, some pulsar scattering appears dominated by a single sheet, leading to the prominent inverted arclets (Stinebring et al. 2001).

2.1 Archival data of B0834+06

Our analysis is based on the apex data selected from the secondary spectrum of pulsar B0834+06 in B10, which was observed as part of a 300 MHz global VLBI project on 2005 November 12, with GBT (GB), Arecibo (AR), Lovell and Westerbork (WB) telescopes. The GB-AR and AR-WB baselines are close to orthogonal and of comparable lengths, resulting in relatively isotropic astrometric positions. Information from each identified apex includes delay τ, delay rate (differential frequency $f_{\rm D}$), relative Right Ascension $\Delta\alpha$ and relative declination $\Delta\delta$. Data of each apex are collected from four dual circular polarization 8 MHz wide sub-bands spanning the frequency range 310.5–342.5 MHz. As described in B10, the inverse parabolic arclets were fitted to positions of their apexes, resulting in a catalogue of apexes in each sub-band, each with delay and differential frequency. As previously described, the positions of the apexes appear constant across sub-bands. In this work, we first combine the apexes across sub-bands, resulting in a single set of images. We focus on the southern group with negative differential frequency: this grouping appears as a likely candidate for a double lensing screen. However, two groups (with positive/negative differential frequency) appear distinct in both the VLBI angular positions and the secondary spectra. We divide the apex data with negative $f_{\rm D}$ into two groups: in one group, time delay ranges from 0.1 ms to 0.4 ms, which we call 0.4 ms group; and in the other group, time delay at about 1 ms, which we call 1 ms group. In summary, the 0.4 ms group contains 10 apexes in the first two sub-bands, and 14 apexes in the last two sub-bands; the 1 ms group, contains 5, 6, 5 and 4 apexes in the four sub-bands subsequently, with center frequency of each band $f_{\rm band} = 314.5, 322.5, 330.5$ and 338.5 MHz.

We select the equivalent apexes from four sub-bands. To match the same apexes in different sub-bands, we scale the differential frequency in different sub-bands to 322.5 MHz, by $f_{\rm D}(322.5/f_{\rm band})$ MHz. A total of 9 apexes from the 0.4 ms group and 5 apexes from the 1 ms group, were mapped. This results in an estimation for the mean referenced frequency $f = 322.5$ MHz and a standard deviation among the sub-bands, listed in Table 1. The $f_{\rm D}$, τ, $\Delta\alpha$ and $\Delta\delta$ are the mean values of n sub-bands ($n = 3$ for points 4 to 6, and 4 for the rest points), listed in Table 1.

We estimate the error of time delay τ, differential frequency $f_{\rm D}$, $\Delta\alpha$ and $\Delta\delta$ listed in Table 1 from their band-to-band variance:

$$\sigma^2_{\tau,{\rm f_D},\Delta\alpha,\Delta\delta} = \frac{1}{n}\sum_{i=1}^{n}\frac{(x_i-\bar{x})^2}{n-1}, \tag{1}$$

and n is the number of sub-bands. The outer $1/n$ accounts for the expected variance of a mean of n numbers.

2.2 One lens model

2.2.1 Distance to the lens

In the absence of a lens model, the fringe rate, delay and angular position cannot be uniquely related. To interpret the data, we adopt the lensing model of Pen & Levin (2014). In this model, the lensing is due to projected fold caustics of a thin sheet closely aligned to the line of sight. We will list the parameters in this lens model in Table 2.

We define the *effective distance* $D_{\rm e}$ as

$$D_{\rm e} \equiv \frac{2c\tau}{\theta^2}. \tag{2}$$

The differential frequency is related to the rate of change of

Figure 1. Reflection of lights on surface waves. At grazing angles, each wave crest results in an apparent image, resulting in a linear streak of images centered on the unperturbed image location. For example, the red light streak would consist of a single image at its center in the absence of waves. Image copyright Kaitlyn McLachlan, licensed through shutterstock.com image ID 45186139.

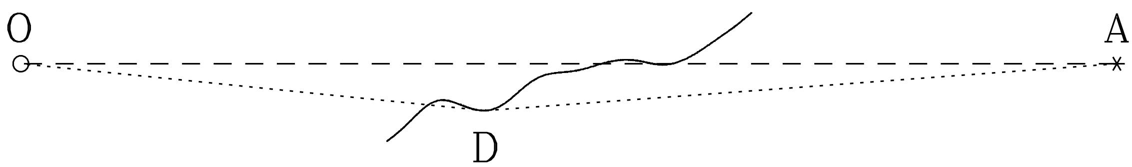

Figure 2. Lensing geometry (reproduced from Pen & Levin (2014) fig. 1). The pulsar is on the right, observer on the left. Each fold of the sheet leads to a divergent projected density, resulting in a lensed image as indicated by the dotted line. See text for details.

Table 2. Parameters for double lens model

$D_{1\mathrm{e}}$	Effective Distance of 0.4 group data
$D_{2\mathrm{e}}$	Effective Distance of 1 ms group data
D_1	Distance of lens 1
D_2	Distance of lens 2
γ	Scattering axis angle of 0.4 ms group[a]
ϵ	Angle of the velocity of the pulsar[a]

[a] The angle is measured relative to the longitude and east is the positive direction.

delay as $f_\mathrm{D} = -f\frac{\mathrm{d}\tau}{\mathrm{d}t}$. The effective distance corresponds to the pulsar distance D_p, if the screen is exactly halfway. In general, $D_\mathrm{e} = D_\mathrm{p}D_\mathrm{s}/(D_\mathrm{p} - D_\mathrm{s})$ for a screen at D_s. Fig. 3 shows two sets of D_p and D_s with common D_e.

When estimating the angular offset of each apex, we subtract the expected noise bias: $\theta^2 = (\Delta\alpha\cos(\delta))^2 + (\Delta\delta)^2 - \sigma^2_{\Delta\alpha} - \sigma^2_{\Delta\delta}$. We plot the θ vs square root of τ in Fig. 4. A least square fit to the distance results in $D_{1\mathrm{e}} = 1044\pm22$ pc for the 0.4 ms group, which we call lens 1 (point 1 is excluded since VLBI astrometry was only known for one subband, thus we cannot obtain the variance nor weighted mean for that point), and $D_{2\mathrm{e}} = 1252\pm49$ pc for the 1 ms group, hereafter lens 2. The errors, and uncertainties on the error, precludes a definitive interpretation of the apparent difference in distance. At face value, this indicates that the lens 2 is closer to the pulsar, and we will use this as a basis for the

label	$\theta_\parallel$(mas)	$f_{\rm D}$(mHz)	τ(ms)	$\Delta\alpha$(mas)	$\Delta\delta$(mas)	t_0(d)
1	−17.22	−26.1(4)	0.3743(6)	6.2	−11.9	−107
2	−16.36	−24.9(4)	0.3378(3)	8.0(4)	−14.5(8)	−101
3	−16.08	−24.6(4)	0.327(3)	7.2(6)	−13.9(4)	−99.0
4	−14.45	−22.3(5)	0.2633(3)	6.1(4)	−13.1(7)	−88.1
5	−13.68	−21.2(6)	0.236(2)	5.1(4)	−12.7(5)	−83.3
6	−13.27	−20.4(5)	0.222(3)	5.8(4)	−11.8(1)	−81.4
7	−12.21	−18.9(2)	0.188(2)	5.5(6)	−10.8(6)	−74.2
8	−10.58	−16.8(3)	0.1412(9)	3.9(6)	−10.0(4)	−62.8
9	−8.18	−12.9(2)	0.0845(5)	2.8(3)	−8.6(4)	−48.7
1’	···	−43.1(4)	1.066(5)	−8(3)	−24(2)	−185
2’	···	−41.3(5)	1.037(3)	−14(1)	−23(3)	−188
3’	···	−40.2(6)	1.005(8)	−14(1)	−22.3(5)	−187
4’	···	−38.3(6)	0.9763(9)	−14(1)	−20.6(3)	−190
5’	···	−35.1(5)	0.950(2)	−15(1)	−21(1)	−202

Table 1. 0.4 ms and 1 ms reduced apex data. The upper part of the table list the 0.4 ms group data, while the 1 ms group lie in the lower part of the table. Observation data include the differential frequency $f_{\rm D}$, time delay τ (τ_1 for 0.4 ms group and τ_2 for 1 ms group); $\Delta\alpha$ and $\Delta\delta$ are from the VLBI measurement (there is only one matched position for point 1, thus no error). t_0 is the time at constant velocity for an apex to intersect the origin at constant speed along the main scattering parabola. More details in Section 2.1 and Section 2.2.2.

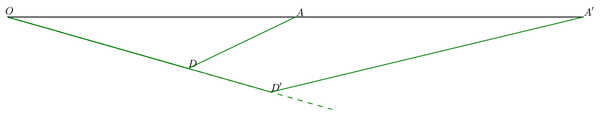

Figure 3. A single refracted light path showing the distance degeneracy. The primed and un-primed geometries result in the same observables: delay τ and angle θ. O denotes the observer; A and A' are denote the positions of the pulsar; D and D' denote the positions of the refracted images on the interstellar medium. The un-primed geometry corresponds to a pulsar distance $D_{\rm p} = |AO| = 620$ pc, while the primed geometry has twice the pulsar distance.

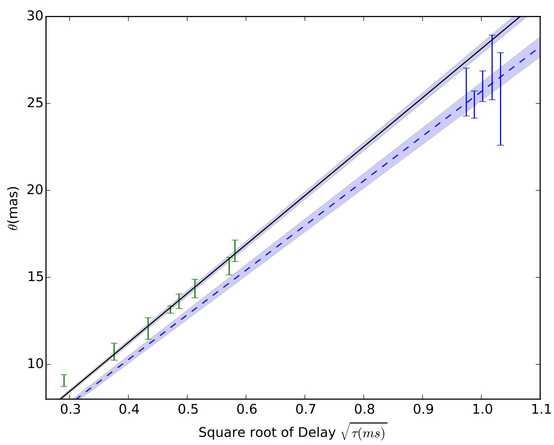

Figure 4. θ vs $\sqrt{\tau}$. Two separate lines through the origin were fitted to the points sampled among the 0.4 ms group and 1 ms group. The solid line is the fitted line of the 0.4 ms positions, where $D_{1\rm e} = 1044$ pc with an error region of $\sigma_D = 22$ pc. The dashed lines are the fitted lines of the 1 ms position, where $D_{2\rm e} = 1252$ pc with an error region $\sigma_D = 49$ pc.

model in this paper. The distances are slightly different from those derived in B10, which is partly due to a different subset of arclets analysed. We discuss consequences of alternate interpretations in Section 2.4. The pulsar distance was directly measured using VLBI parallax to be $D_{\rm p} = 620\pm60$ pc, described in more detail in Section 3. We take $D_{1\rm e} = 1044$ pc, and the distance of lens 1 D_1, where 0.4 ms group scintillation points are refracted, as 389 pc. Similarly, for 1 ms apexes, the distance of lens 2 is taken as 415 pc, slightly closer to the pulsar.

For the 0.4 ms group, we adopt the geometry from B10, assigning these points along line AD as shown in Fig. 5 based solely on their delay, which is the best measured observable. The line AD is taken as a fixed angle of $\gamma = -25^\circ.2$ east north. We use this axis to define $\parallel$ and define $\perp$ by a 90° clockwise rotation.

2.2.2 One lens model

The 0.4 ms group lens solution appears consistent with the premise of the inclined sheet lensing model (Pen & Levin 2014), which predicts collinear positions of lensing images. The time in the last column of Table 1, which we denote as $t_0 = -2\tau f/f_D$, corresponds to the time required for the delay of an arclet to cross the apex of the main parabola.

The collinearity can be considered a post-diction of this model. The precise positions of each image is random, and with 9 images no precision test is possible. The predictive power of sheet model becomes clear in the presence of a second, off-axis screen, which will be discussed below.

2.3 Double lens model

The apparent offset of the 1 ms group can be explained by a second lens screen. The small number of apexes at 1 ms suggests that the second lens screen involves a single caustic at a different distance. One expects each lens to re-image the full set of first scatterings, resulting in a number of apparent images equal to the product of number of lenses

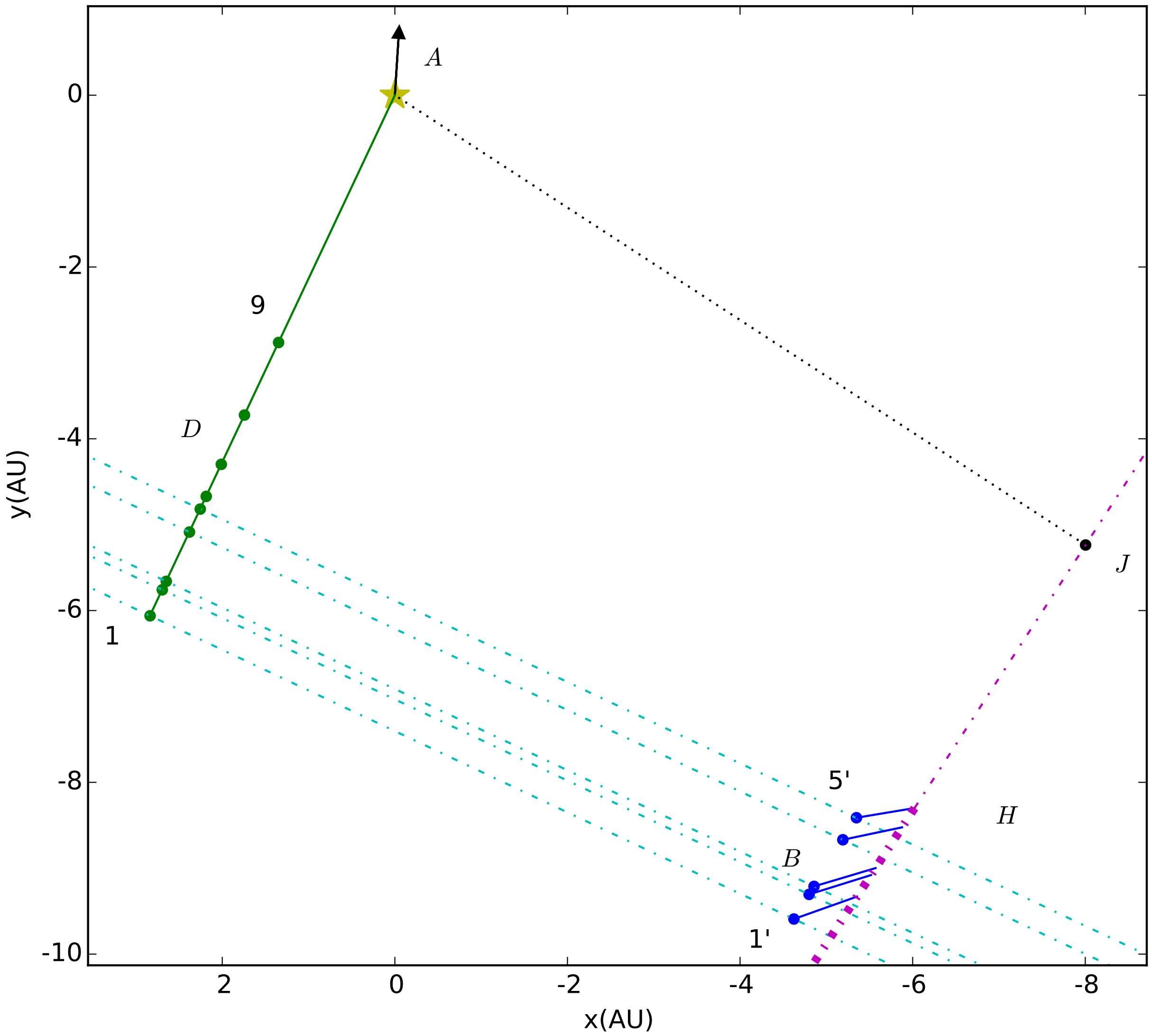

Figure 5. Angular positions of 0.4 ms and 1 ms group data in one lens model and double lens model. The axes represent the relative distance to the un-refracted pulsar in Right Ascension (calculated by $x = \Delta\alpha\cos(\delta)D$ and D represent the distance of the object to the observer) and declination (calculated by $y = \Delta\delta D$, with D defined previously) directions, on a 2D plane that is transverse to the line of sight. On the left side, the points marked with letter D labelled from 1 to 9, are the derived positions from the time delays of 0.4 ms group in one lens model. 389 pc away from the observer, the green solid line aligns the 0.4 ms apexes positions, with a angle $\gamma = -25^\circ.2$ east of north. The points on the right side, mark the first and second refraction points in double lens model. The unobservable points denoted as letter H, are the calculated positions on lens 2 from the 1 ms group; the observed apparent positions denoted as letter B, are the second refraction on lens 1. These two piles of refracted images are connected by the short solid lines. The long dash dotted line passing through J is the inferred geometry of the second lens. Its thicker portion has formed a full caustic, while the thinner portion are sub critical. The dash dotted lines, constructed perpendicular to the AD scattering axis, denote the caustics of lens 1. The dotted line on the top right is perpendicular to the magenta dash dotted line, intersecting at J. The relative model pulsar-screen velocity is 185.3 km s^{-1}, with an angle $\epsilon = -3^\circ.7$ east of north, is marked with an arrow from the star, point A, at the top of the figure.

in each screen. In the primary lens system, the inclination appears such that typical waves form caustics. The number of sheets at shallower inclination increases as the square of the small angle. A 3 times less inclined sheet occurs 9 times as often. If a 1-σ wave forms a caustic in the primary lens, a 3 times less inclined surface only forms caustics for 3-σ waves, which occur two hundred times less often. Thus, one expects such sheets to only form isolated caustics, which we expect to see occasionally. Three free parameters describe a second caustic: distance, angle, and angular separation. We fix the distances from the effective VLBI distance (D_1 and D_2), and fit the angular separations and angles with the 5 delays of the 1 ms group.

2.3.1 *Solving the double lens model*

Apexes 1'–5' share a similar 1 ms time delay, suggesting they are lensed by a common structure. We denote the position of the pulsar point A, positions of the lensed image on lens 2 point H, positions of the lensed image on lens 1 point B, position of the observer point O, $AJ \perp HJ$ at intersection point J, $HF \perp BD$ at intersection point F, $BG \perp HJ$ by intersection point G, for easier discussion.

A 3D schematic of two plane lensing by linear caustics is shown in Fig. 6.

First, we calculate the position of J. We estimate the distance of J from the 1 ms θ–$\sqrt{\tau}$ relation (see Fig. 4). We determine the position of J by matching the time delays of point 4' and point 1', which is marked in Fig. 5. The long dash dotted line on the right side denotes the inferred geometry of lens 2, and by construction vertical to AJ.

The second step is to find the matched pairs of those two lenses. By inspection, we found that the 5 furthest points in 0.4 ms group match naturally to the double lens images. These five matched lines are marked with cyan dash dotted lines in Fig. 5 and their values are listed in the second column in Table 4. They are the located at a distance 389 pc away from us. Here we define three distances:

$$\begin{aligned} D_{p2} &= 620 \text{ pc} - 415 \text{ pc} = 205 \text{ pc}, \\ D_{21} &= 415 \text{ pc} - 389 \text{ pc} = 26 \text{ pc}, \\ D_1 &= 389 \text{ pc} - 0 \text{ pc} = 389 \text{ pc}, \end{aligned} \tag{3}$$

where $D_{\rm p2}$ is the distance from the pulsar to lens 2, D_{21} is the distance from lens 2 to lens 1, and D_1 is the distance from lens 1 to the observer.

Fig. 7 and Fig. 8 are examples of how light is refracted on the first lens plane and the second lens plane. We specifically choose the point with $\theta_{\parallel} = -17.22$ mas, which refer point 1' on lens 2 as an example. Considering the velocity of the photon parallel to the lens plane before and after refraction should be equal, we solve the solutions in double lens model using:

$$\begin{aligned} \frac{JH}{D_{\rm p2}} &= \frac{HG}{D_{21}}, \\ \frac{FB}{D_{21}} &= \frac{BD}{D_1}. \end{aligned} \tag{4}$$

The solved positions are plotted in Fig. 5, and respective time delays and differential frequencies are listed in Table 4. The error of time delay τ in double lens model is taken as

$$(\frac{\sigma_{\tau_i}}{\tau_{2i}})^2 = (\frac{\sigma_{\tau 1i}}{\tau_{1i}})^2 + (\frac{\sigma_{\tau 2i}}{\tau_{2i}})^2 + (\frac{\sigma_{\tau 2j}}{\tau_{2j}})^2, \tag{5}$$

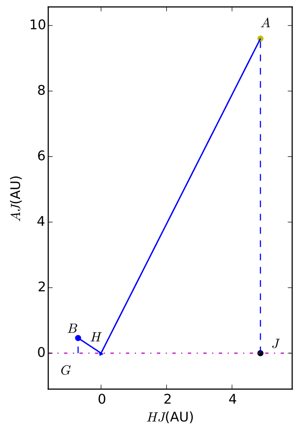

Figure 7. Refraction on lens 2. A is the position of the pulsar. H is the lensed image on lens 2. B is the lensed image on lens 1. $AJ \perp HJ$ and $BG \perp HJ$. The values are illustrated for point 1'.

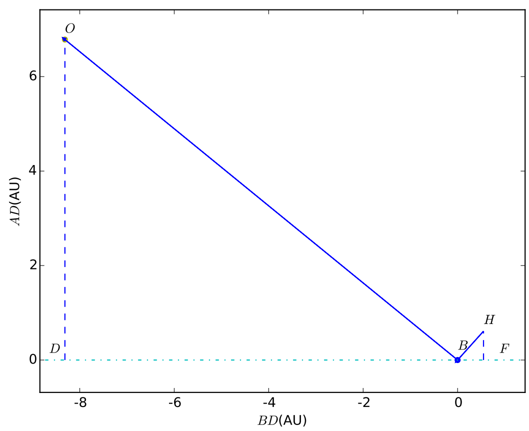

Figure 8. Refraction on lens 1. H is the lensed image on lens 2. B is the lensed image on lens 1. O is the position of the observer. $HF \perp DF$ and $OD \perp HJ$. As in the previous figure, the values are illustrated for point 1'.

where τ_1 and $\sigma_{\tau 1}$ represent the time delay and its error from the 0.4 ms group on lens 1, τ_2 and $\sigma_{\tau 2}$ represent the time delay and its error from respective 1 ms group on lens 2. And τ_{2j} is the τ_2 for the nearest point in reference in Table 4 and $\sigma_{\tau 2j}$ is its error: for point $i = 5', 3'$, $j = 4'$; for point $i = 2'$, $j = 1'$.

For the error of differential frequency $f_{\rm D}$, we add the error of the reference point (point 4') to the error of each other measured point:

$$(\frac{\sigma_{f_i}}{f_{{\rm D}i}})^2 = (\frac{\sigma_{f{\rm D}i}}{f_{{\rm D}i}})^2 + (\frac{\sigma_{f{\rm D4'}}}{f_{\rm D4'}})^2 \tag{6}$$

where $f_{\rm D4'}$ and $\sigma_{f_{\rm D4'}}$ are the differential frequency and its error of the point in the fourth row in Table 4.

2.3.2 *Comparing with observations*

In order to compare τ, we calculate time delay $\tau_{\rm M}$ for these five points, and list the results in Table 4. For points 4' and

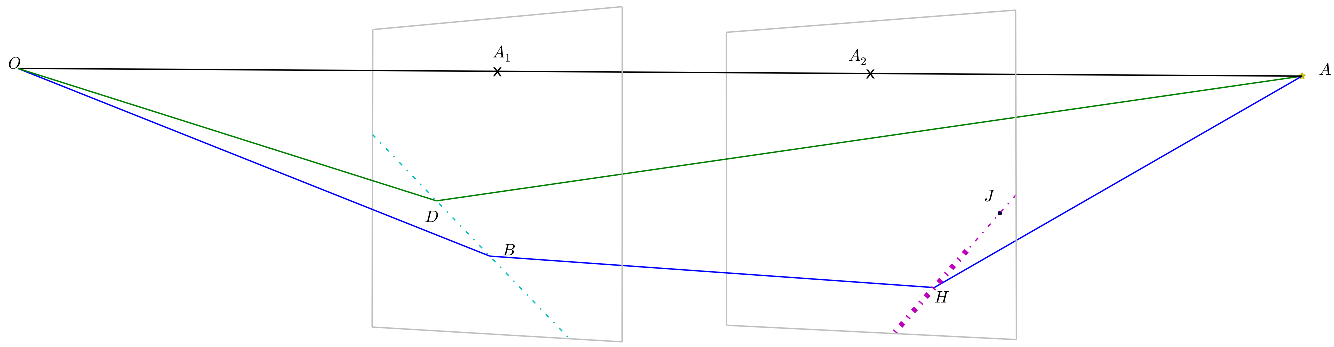

Figure 6. A 3D schematic of light path when light is double refracted. Two planes from left to right are the plane of lens 1, and the plane of lens 2. The dash dotted lines represent the projected line-like fold caustics. Light goes from A (pulsar) to the first refracted point H on lens 2 (line HJ, magenta dash dotted line), and then the second refracted point D, the image we observe, on lens 1 (line BD, cyan dash dotted line), and finally the observer O. Dash dotted lines show the light path of single deflected light path ($A-D-O$). The crosses (A_1 on plane 1, and A_2 on plane 2) denote intersection of the un-deflected light through the lensing sheet. D and J are the closest point of the lens caustic to the un-deflected path, which are the loci of single deflection images. Thus, $A_2J \perp HJ$, and $A_1D \perp BD$. The thick line on plane 2 indicates the real caustic, while the thin continuation indicates the extrapolated continuation beyond the cusp/swallowtail.

1', they fit by construction since we use these to calculate the position of J; for the remaining three points, all of the results are within 3-σ of the observed time delays.

To compare differential frequency $f_{\rm D}$, we need to calculate the velocity of the pulsar and the velocity of the lens. We take the lenses to be relative static, and solve the velocity of the pulsar relative to the lens (in geocentric coordinate). The pulsar has two velocity components, and the two 1-D lenses effectively determine one component each. For $v_\parallel$, we derive the velocity 172.4 ± 2.4 km s^{-1} from $f_{\rm D}$ of point 1 in 0.4 ms group. The direct observable is the time to crossing of each caustic, denoted t_0 in Table 1.

To calculate $v_\perp$, we choose the point 4', which has the smallest errorbar of differential frequency. With $v_\perp$ to be 67.9 ± 2.8 km s^{-1}, we find $v_{\rm tot} = 185.3 \pm 3.3$ km s^{-1}, with an angle $\epsilon = -3^\circ.7$, which is west of north. This represents the pulsar-screen velocity relative to the earth. We can further transform this into the local standard of rest (LSR) frame to interpret the velocities in a galactic context. The model derived and observed velocities (heliocentric and LSR) are listed in Table 3. The direction of the model velocity is marked on the top of the star in Fig. 5.

With this velocity of the pulsar, we calculate the differential frequency $f_{\rm M}$ of points 5',3',2' and 1'. Results are listed in Table 4. The calculated results all lie within the 3-σ error intervals of the observed data.

The reduced χ^2 for time delay τ is 1.5 for 3 degrees of freedom and 2.2 for $f_{\rm D}$ for 4 degrees of freedom. This is consistent with the model.

Within this lensing model, we can test if the caustics are parallel. Using the lag error range of double lensed point 4 (the best constrained), we find a 1-σ allowed angle of 0.4 degrees from parallel with the whole lensing system. This lends support of a highly inclined sheet, probably aligned to better than 1 per cent.

2.3.3 Discussion of double lens model

For the 1 ms group, lens 2 only images a subset of the lens 1 images. This could happen if lens 1 screen is just under the critical inclination angle, such that only 3-σ waves lead to a fold caustic. If the lens 2 was at a critical angle, the chance of encountering a somewhat less inclined system is of order unity. More surprising is the absence of a single refraction image of the pulsar, which is expected at position J. This could happen if the maximum refraction angle is just below critical, such that only rays on the appropriately aligned double refraction can form images. We plot the refraction angle β in the direction that is transverse to the first lens plane in Fig. 9. The data spans about 10 per cent in frequency, making it unlikely that single lens image J would not be seen due to the larger required refraction angle. Instead, we speculate that the fold caustic terminates near double lens image 5', and thus only intersections with the closer lens plane caustic south of image 5' are double lensed.

This is a generic outcome of a swallowtail catastrophe (Arnold 1990). In this picture, the sheet just starts folding near point 5'. North of point 5', no fold appears in projection. Far south of point 5', a full fold exhibits two caustics emanating from the fold cusp. Near the cusp the magnification is the superposition of two caustics, leading to enhanced lensing and higher likelihood of being observed.

We denote t_1 the time for the lensed image on lens 2 to move from point H to point J. From our calculation, 59 d earlier the single lensed pulsar image J would have appeared overlayed on pre-image H_5 of point 5'; and 78 d before 2005 November 12, it overlayed on H_1. The model predicts the presence of a single lensed image refracted at these points, in addition to the double lensed images.

Parameter	$\mu_{\alpha*}$(mas yr^{-1})	μ_δ(mas yr^{-1})	μ_{l*}(mas yr^{-1})	μ_b (mas yr^{-1})	v_{l*} (km s^{-1})	v_b (km s^{-1})
model pulsar-screen velocity	-5.30 ± 1.11	61.97 ± 1.11	-56.45	22.23	···	···
VLBI pulsar proper motion	2.16 ± 0.19	51.64 ± 0.13	-46.69	28.02	-137.24	82.34
Screen motion	···	···	9.76	5.79	18.00	10.68

Table 3. Summary of velocities in double lens model. The velocities listed in equatorial coordinates are the relative velocity in heliocentric system, while the velocities in galactic coordinates are the relative velocities in LSR (Local Standard of Rest). $\mu_{\alpha*} = \Delta\alpha\cos(\delta)/t$ and $\mu_{l*} = \Delta l\cos(b)/t$, for we moved the center position from $(\Delta\alpha, \Delta\delta)$ or (l, b) to (0,0). v_{l*} and v_b are the linear velocities relative to the LSR. The screen is only moving slowly (~ 21 km s^{-1}). Ellipses reflect the unobserved and frame dependent parameters.

label	$\theta_\parallel$ (mas)	τ_2(ms)	σ_τ(ms)	$\tau_{\rm M}$(ms)	$f_{\rm D}$(mHz)	σ_f(mHz)	$f_{\rm M}$(mHz)	t_1(d)
1'	-17.22	1.0663	0.0050	1.0663*	-43.08	0.84	-42.26	-78
2'	-16.36	1.0370	0.0059	1.0362	-41.27	0.88	-41.04	-73
3'	-16.08	1.005	0.011	1.027	-40.17	0.87	-40.64	-72
4'	-14.45	0.9763	0.00088	0.9763*	-38.31	0.64	-38.31†	-63
5'	-13.68	0.9495	0.0094	0.9550	-35.06	0.78	-37.21	-59

Table 4. Comparison of time delay τ and the differential frequency $f_{\rm D}$ of the observation and the model fitting result in the double lens model. $\theta_\parallel$ denotes the angular offsets of the corresponding images at lens 1. The values with star symbols on them are the points that we use to calculate the position of J and the point with a † symbol is the point that we use to calculate the transverse velocity of the pulsar $v_\perp$. They agree with data by construction. The last column, t_1 is the time that the lensed image on lens 2 to move from point H to point J, which is also defined in Section 2.3.3.

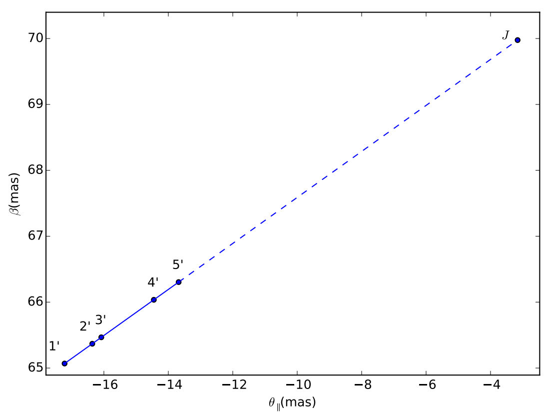

Figure 9. Deflection angle $\beta = \pi - \angle$AHB on lens 2. Point J denotes the expected position to form a single refraction image, which was not observed. The small change in angle relative to the observed images precludes a finite refraction cut-off, since the data spans 10 per cent bandwidth, with a 20 per cent change in refractive strength. We propose a swallowtail caustic as the likely origin for the termination of the second lens sheet.

2.4 Distance Degeneracies

With two lens screens, the number of observables increases: in principle one could observe both single reflection delays and angular positions, as well as the double reflection delays and angular positions. Three distances are unknown, equal to the number of observables. Unfortunately, these measurements are degenerate, which can be seen as follows. From the two screens $i = 1, 2$, the two single deflection effective distance observables are $D_{i{\rm e}} \equiv 2c\tau_i/\theta_i^2 = D_i^2(1/D_i + 1/D_{{\rm p}i})$. A third observable effective distance is that of screen 2 using screen 1 as a lens, $D_{21{\rm e}} = D_1^2(1/D_1 + 1/D_{21})$, within the triangle that is formed by lens 1, lens 2 and the observer. That is also algebraically derivable from the first two relations: $D_{21{\rm e}} = D_{1{\rm e}}D_{2{\rm e}}/(D_{2{\rm e}} - D_{1{\rm e}})$. The light path is shown in Fig. 10.

In this archival data set, the direct single lens from the further plane at position J is missing. It would have been visible 59 d earlier. The difference in time delays to image J and the double reflection images would allow a direct determination of the effective distance to lens plane 2. Due to the close to 90° angle $\angle\, DAJ$ between lenses, the effect would be about a factor of 10 ill conditioned. With sufficiently precise VLBI imaging one could distinguish if the double refracted images are at position B (if lens 1 is closer to the observer) or position H (if lens 2 is closer to the observer). As described above, we interpret the effective distances to place screen 2 further away.

3 VLBI ASTROMETRY

PSR B0834+06 was observed 8 times with the Very Long Baseline Array (VLBA) between 2009 May and 2011 January. Four 16 MHz bands spread across the frequency range 1406 – 1692 MHz were sampled with 2 bit quantization in both circular polarizations, giving a total data rate of 512 Mbps per antenna. The primary phase calibrator was J0831+0429, which is separated from the target by 2.1 degrees, but the target field also included an in-beam calibrator source J083646.4+061108, which is separated from PSR B0834+06 by only 5′. The cycle time between primary phase calibrator and target field was 5 minutes, and the total duration of each observation was 4 hours.

Standard astrometric data reduction techniques were applied (e.g., Deller et al. 2012, 2013), using a phase calibration solution interval of 4 minutes for the in-beam calibrator source J083646.4+061108. J083646.4+061108 is weak (flux density ∼4 mJy) and its brightness varied on the level of tens of percent. The faintness leads to noisy solutions,

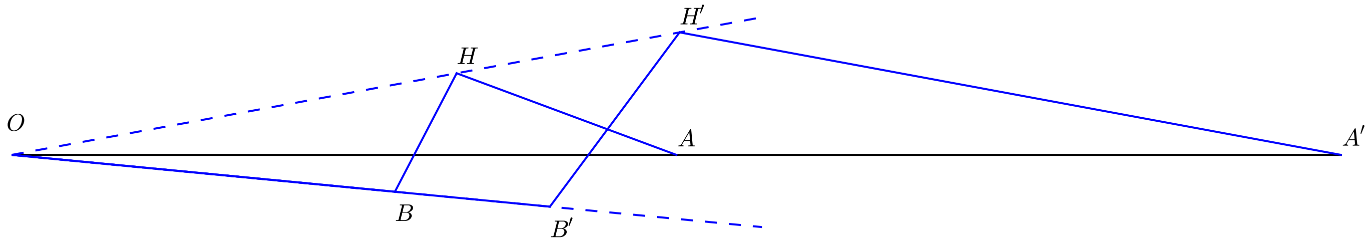

Figure 10. Illustration of double lens degeneracy. As in Fig. 3, all observables are identical for both the prime and un-primed geometries, including all pairwise delays and angular positions.

Table 5. Fitted and derived astrometric parameters for PSR B0834+06.

Reference right ascension (J2000)[a]	08:37:5.644606(9)
Reference declination (J2000)[a]	06:10:15.4047(1)
Position epoch (MJD)	55200
$\mu_{\mathrm{R.A.}}$ (mas yr^{-1})	2.16(19)
μ_{Dec} (mas yr^{-1})	51.64(13)
Parallax (mas)	1.63(15)
Distance (pc)	620(60)
v_{T} (km s^{-1})	150(15)

[a] The errors quoted here are from the astrometric fit only and do not include the ∼1 mas position uncertainty transferred from the in–beam calibrator's absolute position.

and the variability indicates that source structure evolution (which would be translate to offsets in the fitted target position) could be present. Together, these two effects lead to reduced astrometric precision compared to that usually obtained with VLBI astrometry using in-beam calibration, and the results presented here could be improved upon if the observations were repeated using the wider bandwidths and higher sensitivity now available with the VLBA, potentially in conjunction with additional in-beam background sources.

While a straightforward fit to the astrometric observables yields a pulsar distance with a formal error <1 per cent, the reduced χ^2 of this fit is ∼40, indicating that the formal position errors greatly underestimate the true position errors, and that systematic effects such as the calibrator effects discussed above as well as residual ionospheric errors dominate. Accordingly, the astrometric parameters and their errors were instead obtained by bootstrap sampling (Efron & Tibshirani 1991). These results are presented in Table 5.

4 DISCUSSIONS

4.1 Interpretation

The relative motion between pulsar and lens is directly measured by the differential frequency, and not sensitive to details of this model. B10 derived similar motions. This motion is in broad agreement with direct VLBI proper motion measurement, requiring the lens to be moving slowly compared to the pulsar proper motion or the LSR. The lens is ∼ 200 pc above the galactic disk. Matter can either be in pressure equilibrium, or in free-fall, or some combination thereof. In free fall, one expects substantial motions. These data rule out retrograde or radially galactic orbits: the lens is co-rotating with the galaxy. In pressure equilibrium, gas rotates slower as its pressure scale height increases, which appears consistent with the observed slightly slower than co-rotating motion. The modest lens velocities also appear consistent with the general motion of the ISM, perhaps driven by galactic fountains (Shapiro & Field 1976) at these latitudes above the disk. In the inclined sheet model, the waves move at Alfvénic speed, but due to the high inclination, will move sub percent of this speed in projection on the sky, and completely negligible compared to other sources of motion.

Alternative models, for example, evaporating clouds (Walker & Wardle 1998) or strange matter (Pérez-García et al. 2013), do not make clear predictions. One would expect higher proper motions from these freely orbiting sources, larger future scintillation samples may constrain these models.

In order to incline one sheet randomly to better than 1 per cent requires of order 10^4 randomly placed sheets, i.e. many per parsec. This sheet extends for ∼ 10 AU in projection, corresponding to a physical scale greater than 1000 AU. These two numbers roughly agree, leading to a physical picture of magnetic domain boundaries every ∼ 0.1 pc. B0834+06 has had noted arcs for multiple years, perhaps suggesting this dominant lens plane is larger than typical. One might expect to reach the end of the sheet within decades.

A generic prediction of the inclined sheets is a change in rotation measure across the scattering length. Over 1000 AU, one might expect a typical RM (rotation measure) change of 10^{-3} rad/m^2. At low frequencies, for example in LOFAR[1] or GMRT[2], the size of the scattering screen extends another order of magnitude in angular size, and RM changes increase to ∼ 0.01, which is plausibly measurable.

4.2 Possible Improvements

We discuss several strategies which can improve on the solution accuracy. The single biggest improvement would be to monitor over several months, as the pulsar crosses each individual lens, including both lensing systems. This allows a direct comparison of single lens to double lens arclets.

Angular resolution can be improved using longer baselines, for example adding a GMRT-GBT baseline doubles

[1] http://www.lofar.org/
[2] http://gmrt.ncra.tifr.res.in/

the resolution. Observing at multiple frequencies over a longer period allows for a more precise measurement: when the pulsar is between two lenses, the refraction angle β is small, and one expects to see the lensing at higher frequency, where the resolution is higher, and distances between lens positions can be measured to much higher accuracy.

Holographic techniques (Walker et al. 2008; Pen et al. 2014) may be able to measure delays, fringe rates, and VLBI positions substantially more accurately. Combining these techniques, the interstellar lensing could conceivably achieve distance measurements an order of magnitude better than the current published effective distance errors. This could bring most pulsar timing array targets into the coherent timing regime, enabling arc minute localization of gravitational wave sources, lifting any potential source confusion.

Ultimately, the precision of the lensing results would be limited by the fidelity of the lensing model. In the inclined sheet model, the images move along fold caustics. The straightness of these caustics depends on the inclination angle, which in turn depends on the amplitude of the surface waves. This analysis concludes a high degree of inclination, and thus high fidelity for geometric pulsar studies.

5 CONCLUSIONS

We have applied the inclined sheet model (Pen & Levin 2014) to archival apex data of PSR B0834+06. The data is well fit by two linear lensing screens, with nearly plane-parallel geometry. The second screen provides a precision test with 10 observables (5 time delays and 5 differential frequencies) and 3 free parameters (the marked points in Table 4). The model fits the data to non-trivial percent accuracy on each of 7 data points. This natural consequence of very smooth reconnection sheets is an unlikely outcome of ISM turbulence. These results, if extrapolated to multi-epoch observations of binary systems, might result in accurate distance determinations and opportunities for removing scattering induced timing errors. This approach also opens the window to measuring precise transverse motions of the ionized ISM outside the galactic plane.

6 ACKNOWLEDGEMENTS

We thank NSERC for support. We acknowledge helpful discussions with Peter Goldreich and M. van Kerkwijk. We thank Michael Williams for photography help. Siqi Liu thanks Robert Main and JD Emberson for helpful discussions on improving the expression of the content. The National Radio Astronomy Observatory is a facility of the National Science Foundation operated under cooperative agreement by Associated Universities, Inc.

REFERENCES

Arnold V. I., 1990, Singularities of Caustics and Wave Fronts. Springer Netherlands
Boyle L., Pen U.-L., 2012, Phys. Rev. D, 86, 124028
Braithwaite J., 2015, MNRAS, 450, 3201
Brisken W. F., Macquart J.-P., Gao J. J., Rickett B. J., Coles W. A., Deller A. T., Tingay S. J., West C. J., 2010, ApJ, 708, 232
Clegg A. W., Fey A. L., Lazio T. J. W., 1998, ApJ, 496, 253
Deller A. T., Archibald A. M., Brisken W. F., Chatterjee S., Janssen G. H., Kaspi V. M., Lorimer D., Lyne A. G., McLaughlin M. A., Ransom S., Stairs I. H., Stappers B., 2012, ApJ, 756, L25
Deller A. T., Boyles J., Lorimer D. R., Kaspi V. M., McLaughlin M. A., Ransom S., Stairs I. H., Stovall K., 2013, ApJ, 770, 145
Efron B., Tibshirani R., 1991, Science, 253, 390
Kramer M., Stairs I. H., Manchester R. N., McLaughlin M. A., Lyne A. G., Ferdman R. D., Burgay M., Lorimer D. R., Possenti A., D'Amico N., Sarkissian J. M., Hobbs G. B., Reynolds J. E., Freire P. C. C., Camilo F., 2006, Science, 314, 97
Longuet-Higgins M. S., 1960, J. Opt. Soc. Am., 50, 845
Lorimer D. R., Kramer M., 2012, Handbook of Pulsar Astronomy. Cambridge University Press
Pen U.-L., King L., 2012, MNRAS, 421, L132
Pen U.-L., Levin Y., 2014, MNRAS, 442, 3338
Pen U.-L., Macquart J.-P., Deller A. T., Brisken W., 2014, MNRAS, 440, L36
Pérez-García M. Á., Silk J., Pen U.-L., 2013, Physics Letters B, 727, 357
Shapiro P. R., Field G. B., 1976, ApJ, 205, 762
Stinebring D. R., McLaughlin M. A., Cordes J. M., Becker K. M., Goodman J. E. E., Kramer M. A., Sheckard J. L., Smith C. T., 2001, ApJ, 549, L97
Walker M., Wardle M., 1998, ApJ, 498, L125
Walker M. A., Koopmans L. V. E., Stinebring D. R., van Straten W., 2008, MNRAS, 388, 1214